



OPEN

# Numerical simulation and in vitro experimental study of the hemodynamic performance of vena cava filters with helical forms

Yu Xiang Huang<sup>1</sup>, Qi Li<sup>1</sup>, Ming Liu<sup>1✉</sup>, Ming Zhao<sup>1✉</sup> & Ying Chen<sup>2✉</sup>

Inferior vena cava filter (IVCF) implantation is a common method of thrombus capture. By implanting a filter in the inferior vena cava (IVC), microemboli can be effectively blocked from entering the pulmonary circulation, thereby avoiding acute pulmonary embolism (PE). Inspired by the helical flow effect in the human arterial system, we propose a helical retrievable IVCF, which, due to the presence of a helical structure inducing a helical flow pattern of blood in the region near the IVCF, can effectively avoid the deposition of microemboli in the vicinity of the IVCF while promoting the cleavage of the captured thrombus clot. It also reduces the risk of IVCF dislodging and slipping in the vessel because its shape expands in the radial direction, allowing its distal end to fit closely to the IVC wall, and because its contact structure with the inner IVC wall is curved, increasing the contact area and reducing the risk of the vessel wall being punctured by the IVCF support structure. We used ANSYS 2023 software to conduct unidirectional fluid–structure coupling simulation of four different forms of IVCF, combined with microthrombus capture experiments in vitro, to explore the impact of these four forms of IVCF on blood flow patterns and to evaluate the risk of IVCF perforation and IVCF dislocation. It can be seen from the numerical simulation results that the helical structure does have the function of inducing blood flow to undergo helical flow dynamics, and the increase in wall shear stress (WSS) brought about by this function can improve the situation of thrombosis accumulation to a certain extent. Meanwhile, the placement of IVCF will change the flow state of blood flow and lead to the deformation of blood vessels. In in vitro experiments, we found that the density of the helical support rod is a key factor affecting the thrombus trapping efficiency, and in addition, the contact area between the IVCF and the vessel wall has a major influence on the risk of IVCF displacement.

**Keywords** Inferior vena cava filter, Deep venous thrombosis, Pulmonary embolism, Numerical simulation

Pulmonary embolism (PE) causes more than 100,000 deaths each year and has become the third leading cardiovascular disease after coronary heart disease and cerebrovascular disease<sup>1,2</sup>. PE usually originates from deep vein thrombosis (DVT), which is caused by abnormal blood coagulation in deep veins, especially the deep veins of the lower extremities<sup>3–5</sup>. DVT of the lower extremities is responsible for 90% of microemboli in pulmonary embolism<sup>6</sup>. After the microemboli are detached from the clot, they migrate with blood to the right ventricle, where they are pushed into the pulmonary artery and its branches by cardiac contraction, blocking the blood supply to the lungs and resulting in pulmonary circulation disorders, resulting in PE<sup>7–9</sup>. The mechanism of pulmonary embolism is shown in Fig. 1a–c.

For the prevention of pulmonary embolism, IVCF has been widely used and shown to have value in preventing PE<sup>10–12</sup>, and the action mechanism of IVCF is shown in Fig. 1d. since the initial umbrella IVCF proposed by K.M. et al. was applied in the clinic. To date, the thrombus interception rate, simplicity and safety of IVCF have been greatly improved. However, there are issues that need to be addressed. For example, IVCF placed in the

<sup>1</sup>Zhejiang Cancer Hospital, Hangzhou Institute of Medicine (HIM), Chinese Academy of Sciences, Hangzhou 310022, Zhejiang, China. <sup>2</sup>School of Artificial Intelligence, Beijing Institute of Economics and Management, Beijing 100102, China. ✉email: liumingiso@163.com; Zmingys@ucas.ac.cn; chenying2018@pku.edu.cn

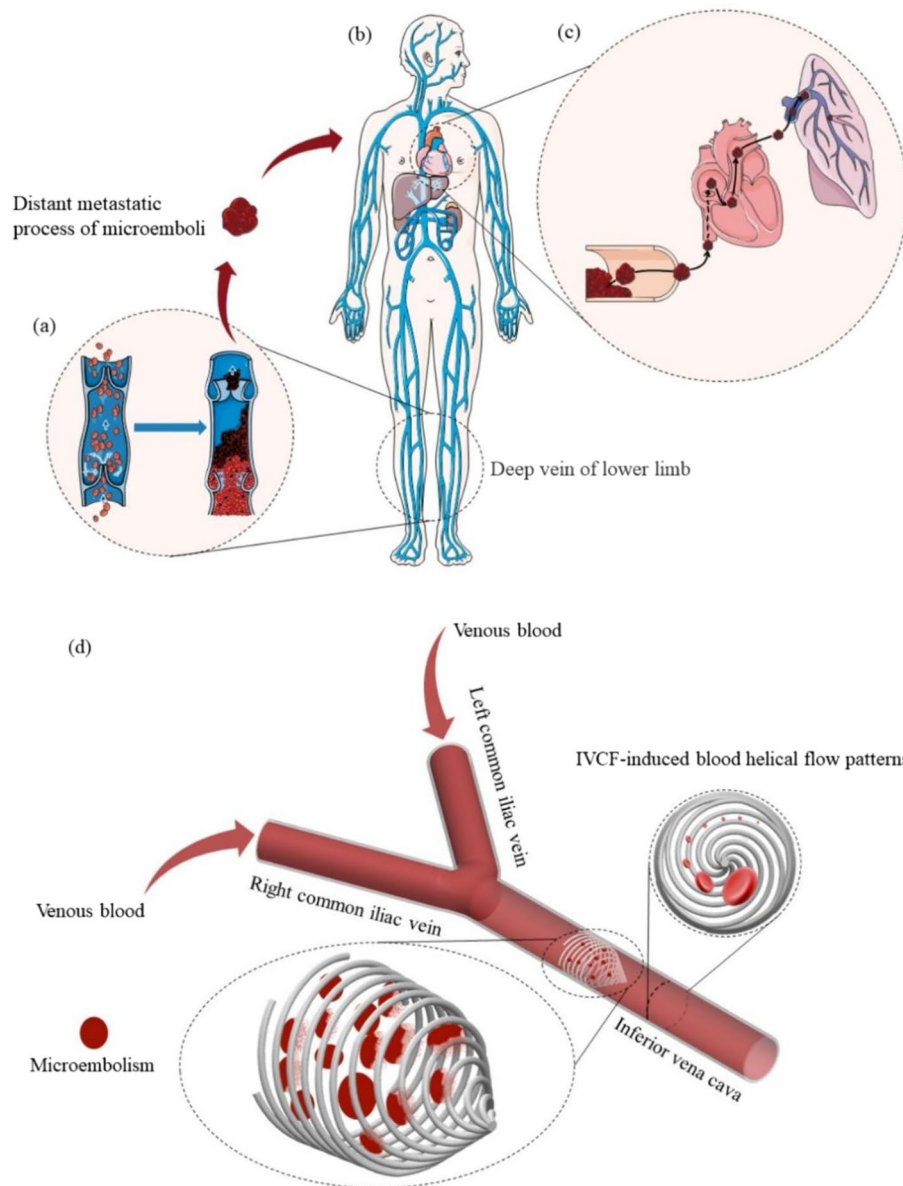


**Figure 1.** Generation mechanism of PE and action mechanism of IVCF (a) Microemboli deposition leading to thrombotic clot formation. (b) The human venous system. (c) Microembolism through the blood circulation into the lungs. (d) The mechanism of IVCF.

body for a long time may result in IVC perforation due to sharp fixed support rods, filter displacement due to blood flow impact, and deep venous embolism of the lower extremity caused by microemboli deposition near the IVCF<sup>13</sup>, leading to severe edema of the lower extremity. Therefore, structural optimization is an important aspect of IVCF design and function improvement.

IVCF implantation also needs to consider its ability to capture thrombi and dissolve the captured thrombi immediately, as well as the risk of IVCF displacement<sup>14</sup>. The performance of IVCF is closely related to hemodynamic factors<sup>15</sup>. Many researchers have performed numerical simulations and in vitro experiments to evaluate the culture and dissolution effects of IVCF. Yang et al.<sup>16</sup> proposed an hourglass-shaped IVCF, which could self-expand and generate enough support to support blood vessels. The results of the simulated thrombus capture experiment in vitro showed that this IVCF had an average capture efficiency of 90% for thrombi with a size of 5 mm × 10 mm. IVCF, with its accumulation of blood clots, causes blockage of itself, which is more of a threat than deep vein clots<sup>17,18</sup>. Therefore, thrombus capture and dissolution are two inseparable and coherent steps, and the unification of these two steps has important clinical value for the prevention of PE. Chen et al.<sup>19</sup> proposed a method to reduce thrombosis accumulation in the vena cava filter. By optimizing the flow mode of blood flow and enhancing the stirring movement of blood, the thrombi trapped in IVCF could be dissolved more quickly, thus facilitating blood flow through IVCF. In vitro experiments showed that thrombosis accumulation in IVCF was reduced by more than 50% under swirling flow conditions. The time it took blood to flow through IVCF

was reduced by 40%, and the helical flow has been regarded as a natural phenomenon in the human arterial system, which can increase the wall shear stress (WSS) of the blood vessels in the thromboembolic area, produce a scouring effect, and reduce the accumulation of thrombus<sup>20,21</sup>. Chen et al. proposed an IVCF that contains a single helical structure and verified the performance of helical structures with different pitches to induce helical flow. The results showed that IVCF with a small pitch helical structure had obvious advantages in improving hemodynamics compared with traditional IVCF<sup>22</sup>. In addition, Chen et al. also proposed an IVCF containing only one single helical structure and compared four different structures with different pitches and morphologies. The results showed that IVCFs with large diameters, large pitches and no conical angle morphology had better hemodynamic performance<sup>23</sup>. However, these IVCFs contain too few helical structures to induce blood flow to greatly produce helical effects. Numerical simulation and in vitro experiments are important approaches for structural design optimization of IVCFs, and the thrombus trapping and dissolution performance of IVCFs, as well as the risk of thrombus accumulation and IVCF displacement, need to be well evaluated for the design and optimization of IVCFs.

In the present investigation, based on the beneficial effect of helical flow<sup>24</sup>, we suggest that IVCFs with helical structures may reduce the risk of thrombotic deposition and blockage by inducing helical flow. A series of IVCFs were proposed, and the performance of these IVCFs was evaluated through numerical simulations and in vitro microthrombus capture experiments. Through CFD numerical simulation<sup>25</sup>, hemodynamic characteristics involving helicity, wall shear stress, blood helicity induced by IVCF, radial stress of IVCF on the blood vessel wall during blood flow, axial impact stress of blood on IVCF, and blood vessel strain were evaluated. In addition, in vitro experiments were carried out to evaluate the capture efficiency of IVCFs with different configurations. Through the combination of numerical simulation and in vitro experiments, the performance of IVCF in all aspects can be effectively evaluated.

## Method and materials

### Model construction

In the present investigation, IVCFs with different configurations were constructed based on research carried out by Gallagher et al. The shape of the cross-section was simplified to be circular, and the hydraulic diameter of the inferior vena cava was set to be constant at 28 mm, which is the maximum indicated IVC diameter for most IVCFs<sup>26</sup>. The cross-sectional diameter of the left and right common iliac veins was a constant 24 mm. The model included the main inferior vena cava and the left and right common iliac veins. The lateral angle of the left common iliac vein was 36.3°, the lateral angle of the right common iliac vein was 20°<sup>27</sup>, the total length of the inferior vena cava was 240 mm, and the lengths of the left and right common iliac veins were 119 mm. In the entire IVC model, the vascular wall thickness was considered as an idealized uniform size of 2 mm (Fig. 2e).

The flow state of fluid is different when it passes through different helical structures. We expect to influence the flow state of fluid by changing the shape of helical structures, so as to find a better hemodynamic state. In this investigation, we constructed four different morphologies of IVCFs using SolidWorks (SolidWorks Corp, Concord, MA). By controlling the variation in diameter with height, three different morphologies of helical filaments were constructed, and subsequently, the circumferential array command was executed to obtain IVCFs with different degrees of radial shrinkage and expansion, and their diameters versus heights are shown in Fig. 2a–c. A control group was then obtained by circumferential array of simple straight filaments (Fig. 2d). We name them EPF, CPF, SPF, and LPF, which stand for the expansion pattern filter (EPF), cone pattern filter (CPF), shrink pattern filter (SPF), and linear pattern filter (LPF), respectively. EPF has a diameter of 30 mm at 0 height, 28 mm at 22.5 mm height, and 0.1 mm at 45 mm height. The diameter of the CPF is 30 mm at 0 height, 14 mm at 22.5 mm height, and 0.1 mm at 45 mm height. SPF has a diameter of 30 mm at 0 height, 8 mm at 22.5 mm height, and 0.1 mm at 45 mm height.

All four IVCFs were 45 mm in length and had a maximum external radius of 15 mm, which was slightly larger than the internal diameter of the IVC. In this case, the LPF was constructed based on the GENI (GENeric NItinol) filter proposed by Riley et al.<sup>28</sup>. It has 16 uniformly spaced support rods with an angle of 23° between the rods and the center axis of rotation, which was modeled to serve as a control group.

### Numerical simulation

In this investigation, all model construction was performed using Solidworks 2021 (SolidWorks Corp, Concord, MA), and all numerical simulation projects were performed using ANSYS 2023 CFD software (ANSYS Inc., Canonsburg, PA). The modules involved in ANSYS include Fluid Flow (Fluent) module and Transient Structural module. In the two modules, the steps of geometric model construction, mesh division, parameter setting and result analysis for fluid domain and solid domain are included respectively.

### Governing equations

Flow simulations were based on the three-dimensional incompressible Navier–Stokes and continuity equations:

$$\rho((\partial \vec{v} / \partial t) + (\vec{v} \cdot \nabla) \vec{v}) = -\nabla p + \nabla \tau \quad (1)$$

$$\nabla \cdot \vec{v} = 0 \quad (2)$$

where  $\vec{v}$  and  $p$  are the fluid velocity vector and pressure, respectively,  $\rho$  is the density of blood ( $\rho = 1050 \text{ kg/m}^3$ ), and  $\tau$  denotes the stress tensor:

$$\tau = 2\eta(\dot{\gamma})D \quad (3)$$

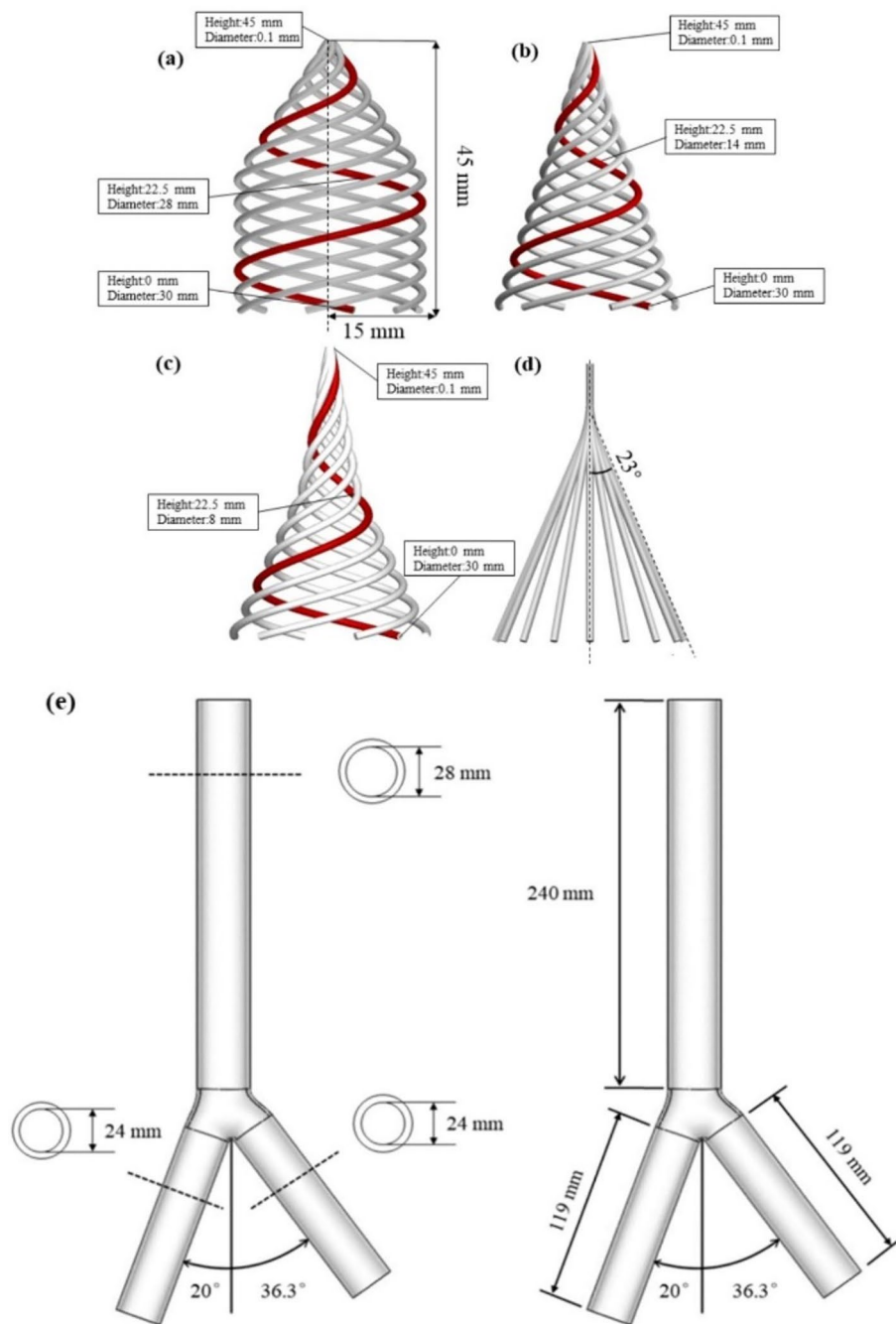


**Figure 2.** Models. (a) Expansion pattern filter (EPF). (b) Conical pattern filter (CPF). (c) Systolic pattern filter (SPF). (d) Linear pattern filter (LPF). (e) Inferior vena cava model.

where  $D$  and  $\dot{\gamma}$  denote the deformation tensor and shear rate, respectively, and  $\eta$  is the viscosity of the blood, which is a function of the shear rate.

In this study, the non-Newtonian properties of blood are considered using the Carreau model:

$$\eta = \eta_{\infty} + (\eta_0 - \eta_{\infty}) \left[ 1 + (\lambda \dot{\gamma})^2 \right]^{\frac{n-1}{2}} \tag{4}$$

where  $\eta_0$  and  $\eta_{\infty}$  are the zero and infinite shear rate viscosities, respectively, and  $\lambda$  is the relaxation time constant. where  $\eta_{\infty} = 3.5 \times 10^{-3}$  Pa s,  $\eta_0 = 5.6 \times 10^{-2}$  Pa s,  $n = 0.3568$ , and  $\lambda = 3.313$  s.

To examine the extent to which the 4 models guide blood rotation, we quantified this metric in terms of helicity density  $H_d$ , which is defined by Eq. (5), and  $H_a$  represents the average helicity, which is defined by Eq. (6):

$$H_d = \vec{v} \cdot (\nabla \times \vec{v}) = \vec{v} \cdot \omega \quad (5)$$

$$H_a = \left( \int_s H_d ds \right) / s \quad (6)$$

Fluid–structure coupling follows the following basic conservation equation:

$$\begin{aligned} \tau_f \cdot n_f &= \tau_s \cdot n_s \\ d_f &= d_s \end{aligned} \quad (7)$$

$n_f$  and  $n_s$  represent the fluid direction vector and solid direction vector, respectively.  $\tau_f$  and  $\tau_s$  represent fluid stress and solid stress, respectively.  $d_f$  and  $d_s$  represent fluid displacement and solid displacement, respectively.

#### Boundary condition

In all numerical simulation projects, steady state is used for calculation, and two blood flow velocities of the inferior vena cava were set to simulate the calculated blood flow velocity, which are 0.06 m/s and 0.10 m/s. The blood was set as incompressible fluid, the blood flow was laminar flow, the dynamic viscosity was  $3.5 \times 10^{-3}$  Pa s, and we set the outlet as the outflow.

Three pairs of contact surfaces were set, namely, blood vessels—filter, blood vessels—blood, and filter—blood, and the contact mode was set as bonding.

#### Material properties

As shown in Table 1, the Young's modulus of the vessel is set at  $5 \times 10^5$  Pa, the density is  $0.941 \times 10^3$  kg/m<sup>3</sup> and the Poisson's ratio is 0.45<sup>29</sup>. Blood density was set at 1050 kg/m<sup>3</sup>. The IVCFs are molded by 3D printing from ABS material with a density of 1053 kg/m<sup>3</sup> and a modulus of elasticity of 2.2 GPa and a Poisson's ratio of 0.394.

#### Mesh

To avoid the influence of the difference in the number of grids on the calculation results and thus lead to the unreliability of the calculation results, this study conducted a grid independence verification, taking the exit flow rate as the judgment standard, and conducted an independent evaluation on 800,000, 1,000,000 and 1,200,000 grids. The evaluation results are as Fig. 3a. The fluid domain (blood) meshing and the solid domain (vessel wall) meshing are shown in Fig. 3b,c.

	Density (kg/m <sup>3</sup> )	Young's modulus (Pa)	Poisson's ratio
Vessel	941	$5 \times 10^5$	0.45
IVCF	1053	$2.2 \times 10^9$	0.394

**Table 1.** Physical parameters of the material.

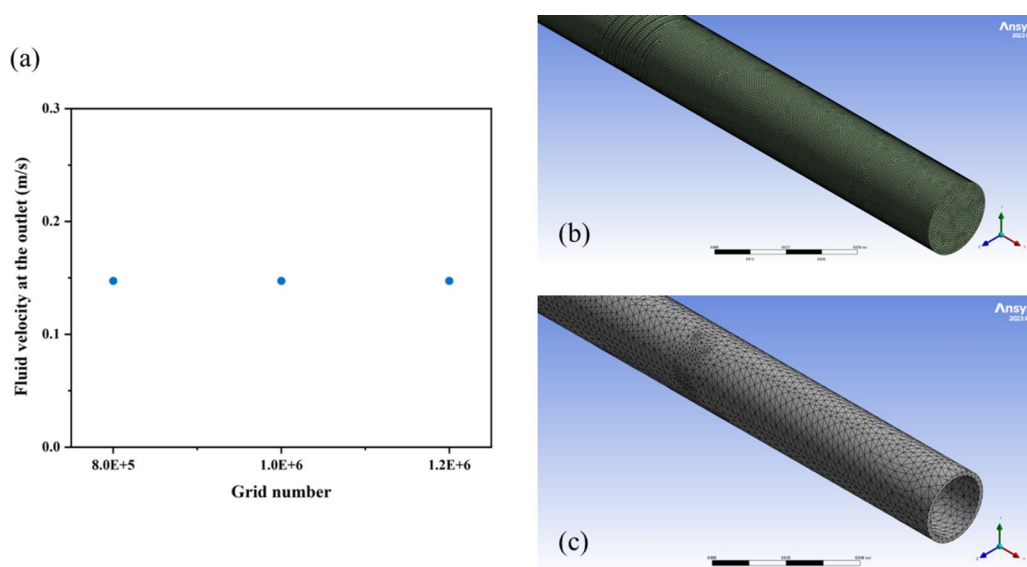


**Figure 3.** Mesh setting. (a) Outlet fluid velocity for three grid numbers. (b) Fluid domain (blood) meshing. (c) Solid domain (vessel wall) meshing.

We investigated the fluid velocity at the outlet for three different grid numbers and found that it did not vary by more than 1%.

## Result

### Flow pattern

To visually display the changes in blood flow morphology when blood passes through IVCF, we studied the state of the blood flow line at two blood flow velocities of 0.06 m/s and 0.10 m/s. As shown in Fig. 4, a helical flow pattern will be induced when blood passes through the EPF, CPF and SPF, while this phenomenon cannot be observed for the LPF. In EPF, CPF and SPF, CPF-induced blood rotation was the most obvious. It is clear that the helical structure plays a major role in inducing blood rotation, and the degree of helical blood varies in the comparison of the first three IVCFs. As seen from the local diagram, the blood velocity varies to different degrees when it passes through the IVCF. In the EPF, CPF and SPF, the increased blood velocity occurs in the inner part of the filter, while in the LPF, the increased blood velocity occurs in the downstream part. In addition, CPF and SPF have an absolute advantage in the function of inducing blood helical flow.

### Helicity

To study the change in helicity of the fluid as it passes through the IVCF, three equally spaced profiles S1, S2, and S3 were set up upstream and downstream of the IVCF, as shown in Fig. 5.

To quantitatively compare the helicity induced by different IVCFs, the average helicity of three isometric profiles, S1, S2 and S3, was extracted, as shown in Fig. 6 and Table 2. The results showed that for the four IVCF types, there was almost no rotation on S1, and the helicity increased from upstream to downstream (S1–S3). Among the four IVCF types, CPF had the best effect on the induction of helical flow of fluid, and LPF had almost no ability to induce helical flow of fluid, with the order of CPF > SPF > EPF > LPF. EPF, CPF and SPF with helical structures can effectively induce blood flow rotation. At the same time, we found that virtually all described IVCF failed to induce helical flow in the upstream blood, whereas the IVCF-induced rotation in the downstream blood was very significant, and even further downstream of IVCF, greater blood flow helicity was produced. The specific helicity is shown in absolute value in Fig. 6 and Table 2. The absolute value of helicity is calculated as follows:

$$H_a = |\vec{v}| \cdot |\vec{\omega}| \quad (8)$$

### Wall shear stress

It can be seen from the simulation results that the four IVCFs are affected by different degrees of WSS (Fig. 7). Obviously, when the blood flow velocity was 0.06 m/s and 0.1 m/s, the average WSS on CPF and SPF was significantly higher than that on EPF and LPF.

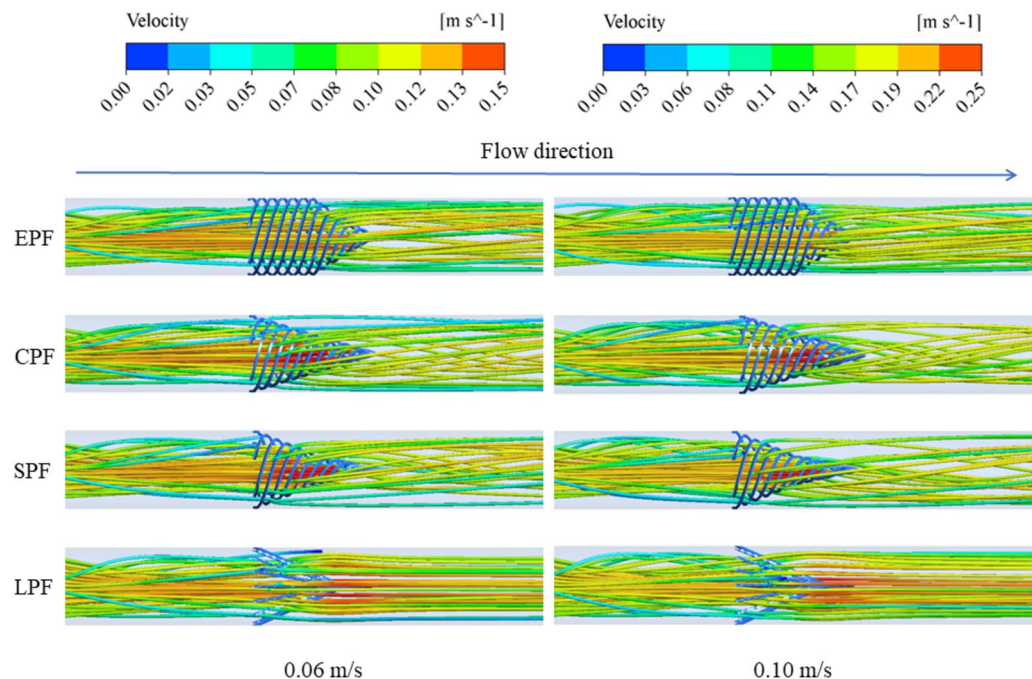


**Figure 4.** Fluid configuration near IVCF.

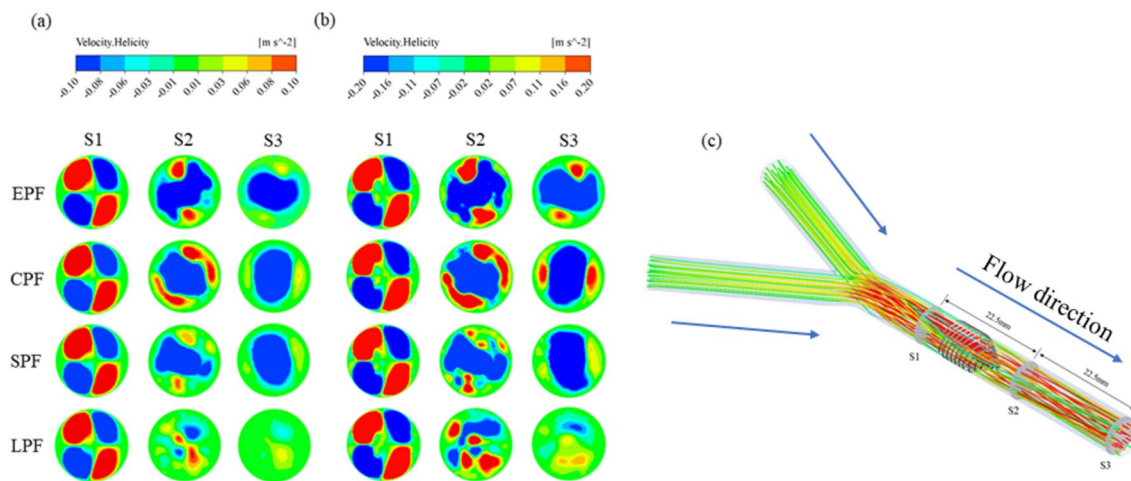


**Figure 5.** Helicity. (a) Helicity at 0.06 m/s blood flow velocity. (b) Helicity at 0.10 m/s blood flow velocity. (c) The positions of the S1, S2, and S3 planes.

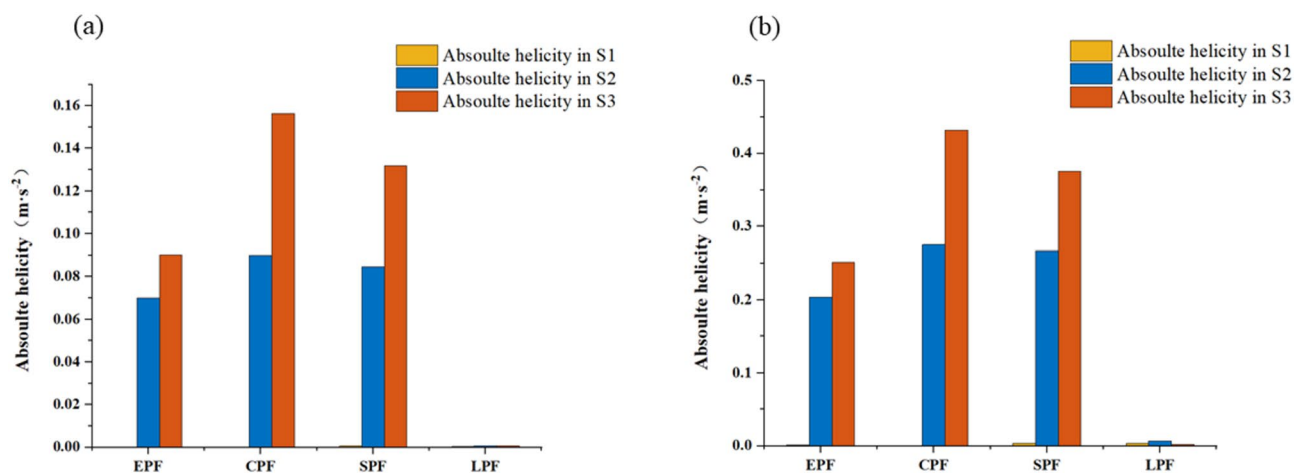


**Figure 6.** Absolute helicity. (a) Helicity at 0.06 m/s blood flow velocity. (b) Helicity at 0.1 m/s blood flow velocity.

	Helicity at 0.06 m/s blood flow velocity (m/s <sup>2</sup> )		Helicity at 0.1 m/s blood flow velocity (m/s <sup>2</sup> )	
	S1	S2	S1	S2
EPF	S1	$1.7 \times 10^{-4}$	S1	$1 \times 10^{-3}$
	S2	$7 \times 10^{-2}$	S2	$2 \times 10^{-1}$
	S3	$9 \times 10^{-2}$	S3	$2.5 \times 10^{-1}$
CPF	S1	$7 \times 10^{-5}$	S1	$6.6 \times 10^{-4}$
	S2	$9 \times 10^{-2}$	S2	$2.8 \times 10^{-1}$
	S3	$1.6 \times 10^{-1}$	S3	$4.3 \times 10^{-1}$
SPF	S1	$5.9 \times 10^{-4}$	S1	$3.3 \times 10^{-3}$
	S2	$8.5 \times 10^{-2}$	S2	$2.7 \times 10^{-1}$
	S3	$1.3 \times 10^{-1}$	S3	$3.8 \times 10^{-1}$
LPF	S1	$3.4 \times 10^{-4}$	S1	$3.8 \times 10^{-3}$
	S2	$7.2 \times 10^{-4}$	S2	$6.9 \times 10^{-3}$
	S3	$6.5 \times 10^{-4}$	S3	$1.9 \times 10^{-3}$

**Table 2.** Absolute helicity on 3 planes.

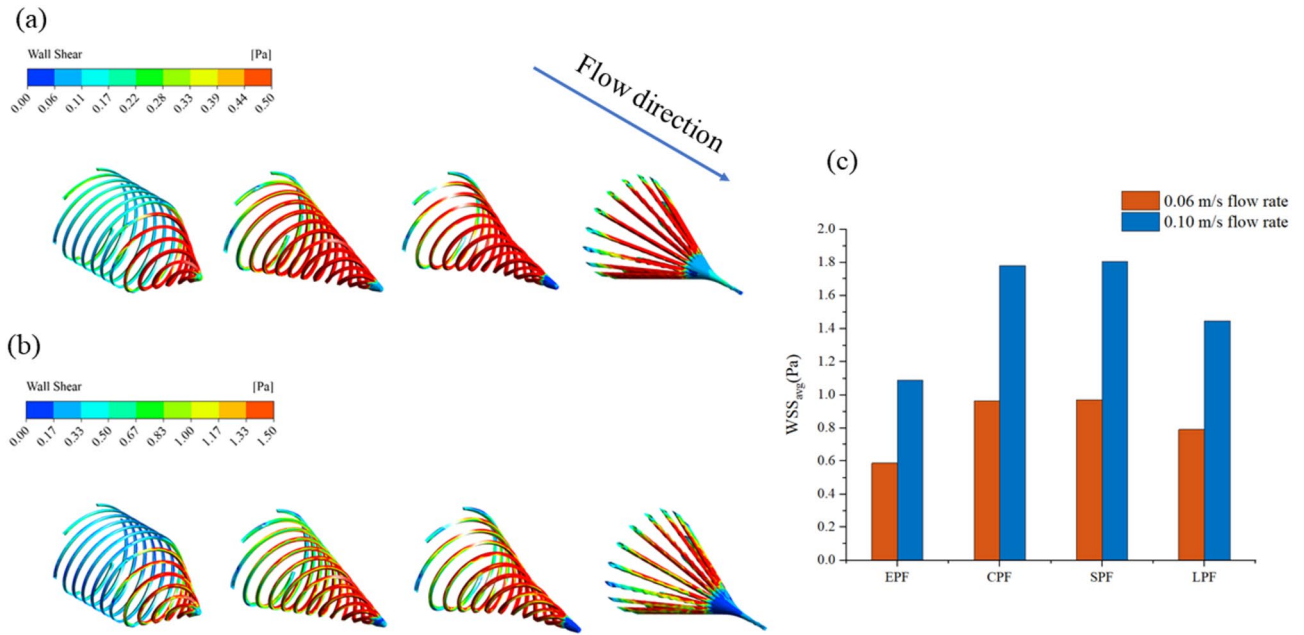


**Figure 7.** Wall shear stress (WSS) of IVCF. (a) WSS distribution of IVCF at 0.06 m/s blood flow velocity. (b) WSS distribution of IVCF at 0.10 m/s blood flow velocity. (c) Average WSS of the four IVCFs.

### Drag force

As shown in Fig. 8, the drag forces on the four IVCFs at inlet blood flow rates of 0.06 m/s and 0.10 m/s were calculated and compared. The drag force is derived from the friction force of the fluid against the IVCF and can be used to determine the risk of IVCF displacement. It was clear that blood had the greatest effect on the resistance of CPF and SPF, followed by LPF, and EPF had the least effect on the resistance of blood flow. When the blood flow velocity is 0.06 m/s, the drag force of fluid on IVCF ranges from  $0.93 \times 10^{-3}$  N to  $1.5 \times 10^{-3}$  N. When the blood flow velocity is 0.1 m/s, the drag force of fluid on IVCF ranges from  $1.7 \times 10^{-3}$  N to  $2.7 \times 10^{-3}$  N. At both flow rates, the maximum drag occurs at CPF:  $1.5 \times 10^{-3}$  N and  $2.7 \times 10^{-3}$  N, respectively.

### Deformation

As shown in Fig. 9, we evaluated the total deformation of the IVC with four IVCF types under blood flow impact at 0.06 m/s and 0.10 m/s. It can be seen from the simulation results that at the blood flow velocity of 0.06 m/s, CPF and SPF caused the most significant deformation ( $3.65 \times 10^{-5}$  m and  $3.22 \times 10^{-5}$  m, respectively), followed by LPF ( $9.59 \times 10^{-6}$  m), and EPF caused the least deformation ( $9.32 \times 10^{-6}$  m). The deformation degree was  $SPF > CPF > LPF > EPF$  from large to small. The large deformation areas of CPF and SPF occupy a longer position, and it can be seen that in CPF and SPF, the upper, middle and downstream vessels where IVCF is located are significantly affected. However, when the flow velocity was 0.1 m/s, the situation was almost the same as when

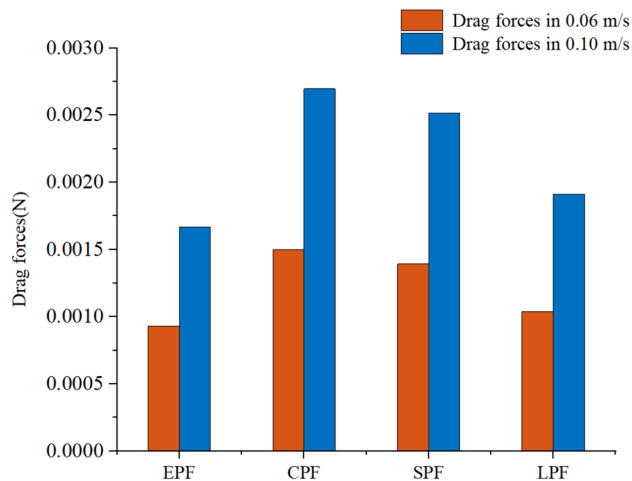


**Figure 8.** Drag forces.



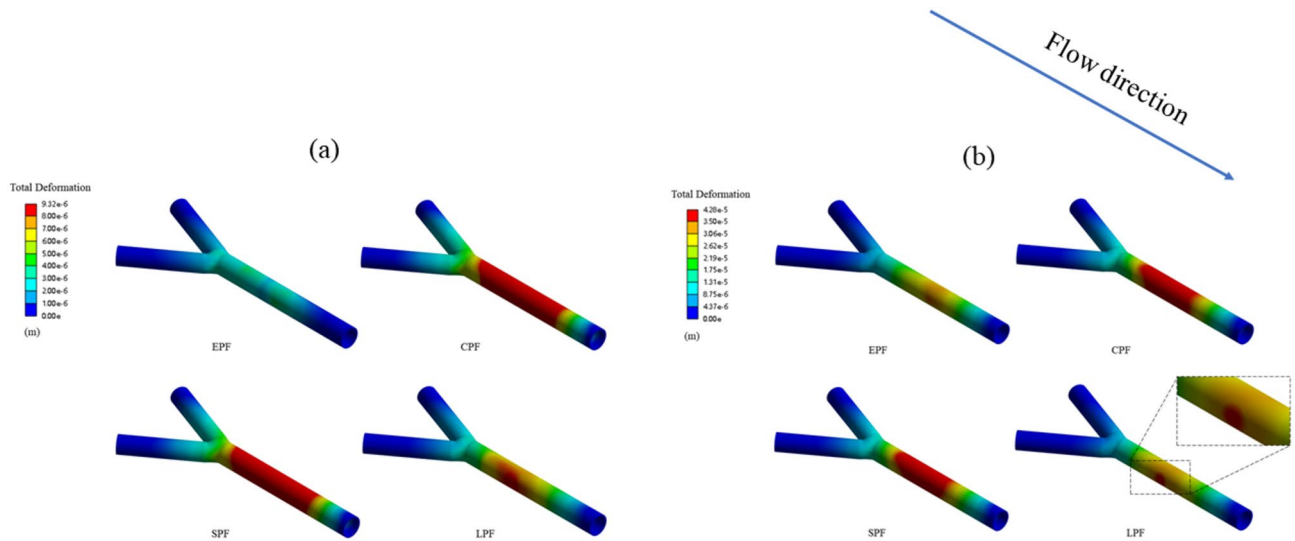


**Figure 9.** The total deformation of IVC caused by four IVCFs. (a) Total deformation of IVC at the blood flow rate of 0.06 m/s. (b) Total deformation of IVC at the blood flow rate of 0.1 m/s.

the flow velocity was 0.06 m/s, and the deformation caused by CPF and SPF was  $9.49 \times 10^{-5}$  m and  $8.42 \times 10^{-5}$  m, respectively. LPF and EPF are  $3.72 \times 10^{-5}$  m and  $4.28 \times 10^{-5}$  m, respectively. IVCF implantation brings a certain degree of deformation to the blood vessels, and different IVCF structures have different deformation effects on the blood vessels. For example, because of the special structure, when the blood flow velocity is 0.06 m/s, the contact surface between the LPF support rod and the blood vessel appears a concentrated deformation area.

### In vitro experiment

In this investigation, we constructed a model of inferior vena cava extracorporeal circulation using 2 mm and 4 mm nylon beads and 3 mm plush beads to simulate microemboli with different shapes and properties<sup>28</sup> and finally obtained the capture rates of these microemboli under different IVCFs. Both IVCF and IVC models are 3D printed (Fig. 10a–d); IVCF is based on acrylonitrile–butadiene–styrene (ABS), while IVC is based on transparent resin. The peristaltic pump is the only power source in this system, the silicone tube is installed in the peristaltic pump, the IVC model is connected to the circulation system through a variable diameter three-way valve, and the silicone tubes at both ends are joined at the liquid storage pool to form a closed loop (Figs. 10e and 13c,d).

### Experimental results

In each IVCF test, we took twenty of each of the three beads for a total of sixty to simulate the microembolus. At a water flow rate of 0.1 m/s, the beads captured by the four kinds of IVCF were collected and counted after a period of 10 min. As shown in Fig. 11, in EPF, we collected two 2 mm nylon beads, twenty 3 mm plush balls and eighteen 4 mm nylon beads. In the CPF, we collected three 2 mm nylon beads, twenty 3 mm pompoms and twenty 4 mm nylon beads. In SPF, we collected six 2 mm nylon beads, twenty 3 mm pompoms and twenty 4 mm nylon beads. In the LPF test, the LPF fell off the fixed position and was washed out of the tube by the water,

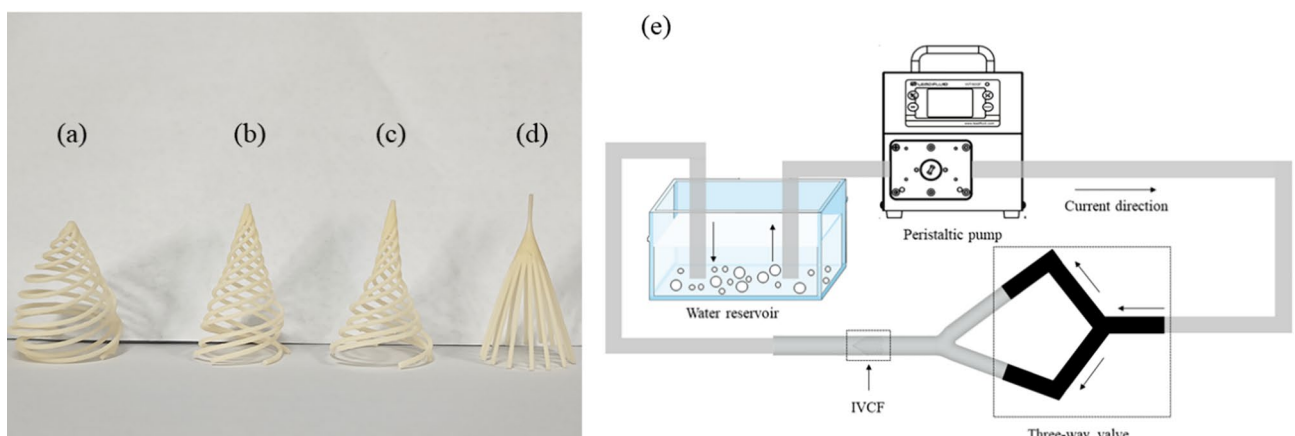


**Figure 10.** 3D printing model and experimental platform of IVCF (a) EPF. (b) CPF. (c) SPF. (d) LPF. (e) IVCF in vitro functional verification platform.

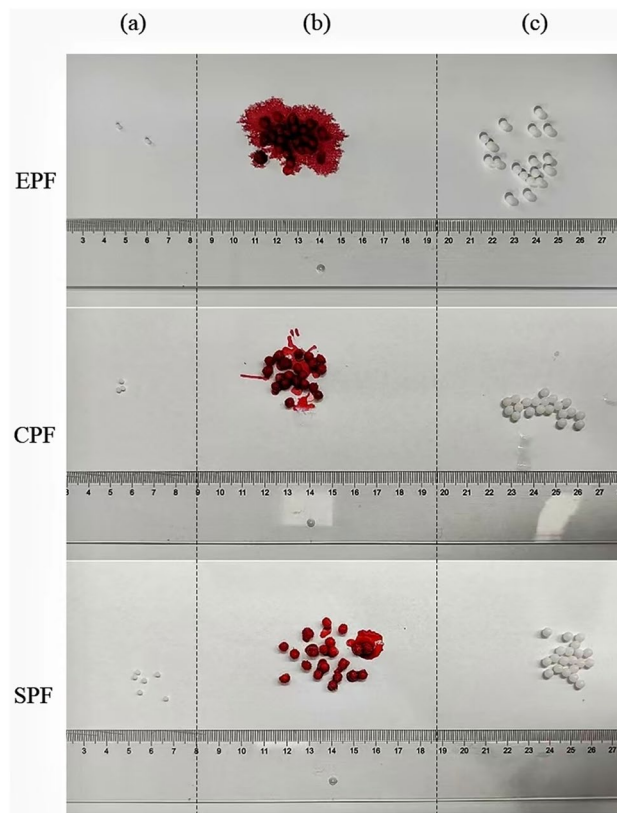


**Figure 11.** Results of the in vitro experiment. (a) 2 mm nylon balls. (b) 3 mm plush ball. (c) 4 mm nylon ball.

so we counted the number of beads it captured as 0. We did the experiment three times to avoid chance in the experiment (Fig. 12). The results show a number of things. First, according to the types of captured beads, we found that the capture rates of hard nylon beads and soft plush beads were almost the same, and even in EPF, the capture rate of soft plush beads was higher than that of hard nylon beads, which was inconsistent with our initial prediction that soft plush beads could easily pass through IVCF because of deformation. When taking the beads off the IVCF and counting, we found that the soft plush beads were clumping together, which we think is the most important reason for the high capture rate. In addition, based on the number of microemboli captured by different IVCFs, we found that the ability to capture 2 mm nylon beads increased with increasing rod density, which is consistent with our expectation, and dense rods were the main reason. Similarly, EPF loses more small microemboli due to its large pore ratio. Finally, we found that except for EPF, the other three IVCFs all had

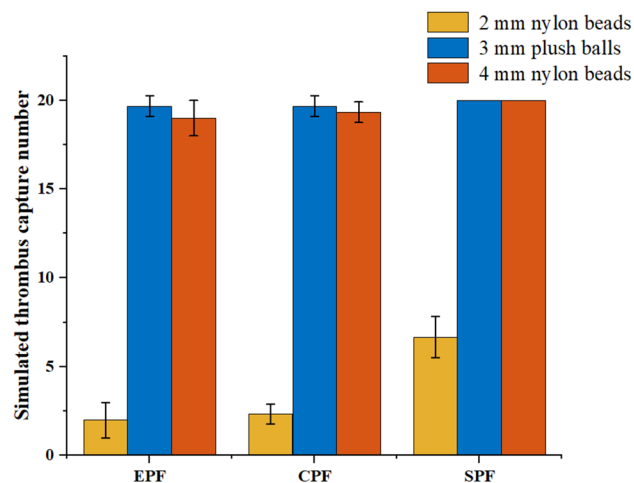


**Figure 12.** Simulated thrombus capture number.

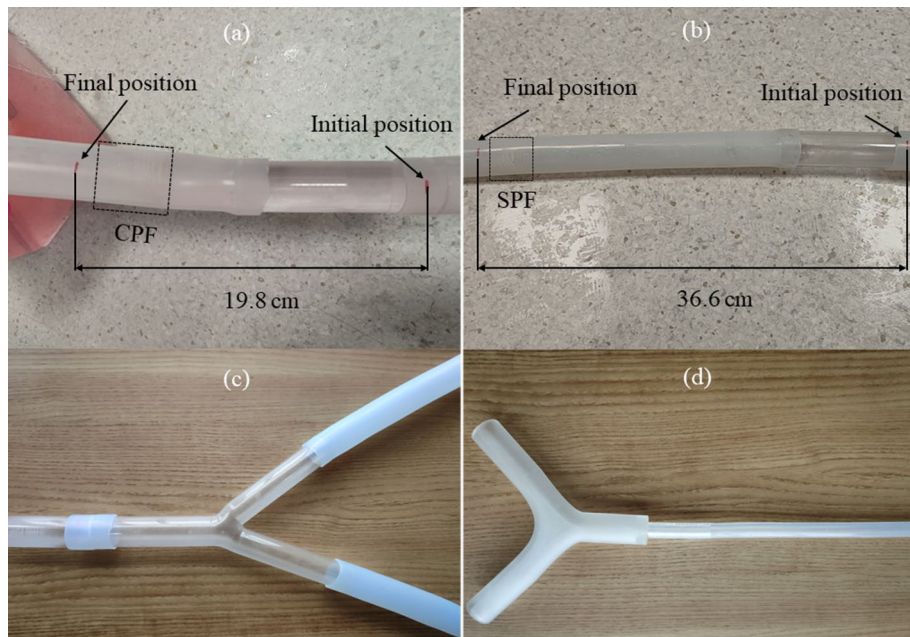


**Figure 13.** IVCF displacement. (a) CPF displacement. (b) SPF displacement. (c) 3D-printed IVC model. (d) 3D-printed three-way valve.

different degrees of displacement under fluid impact (Fig. 13a,b). We believe that this is related to the contact area between the IVCF and the vascular wall, and the radial expansion form of EPF has a good support advantage.

## Discussion

In this investigation, based on the beneficial effect of helical flow, the possibility that helical structure IVCF could reduce thrombus deposition and obstruction by inducing helical flow was proposed by our study group. The performance of these IVCFs was evaluated by numerical simulation and in vitro microthrombus capture experiments. The hemodynamic characteristics, including wall shear stress, blood helicity induced by IVCF, radial stress of IVCF on the blood vessel wall, axial impact stress of blood on IVCF and vascular strain, were evaluated by CFD numerical simulation. In addition, we conducted in vitro experiments to evaluate the capture efficiency of different IVCF configurations. This method using the IVCF structure to induce helical flow to reduce the probability of thrombosis has certain innovative significance.

The curved structure is the key to inducing helical flow<sup>30</sup>. Blood helicity is an important index to evaluate the degree of blood rotation. We believe that the greater the blood helicity is, the smaller the probability of microemboli being deposited in the rotation force field, and the smaller the possibility of thrombosis. In areas of low wall shear stress (WSS) that are prone to thrombosis, another positive effect of increased helicity is an increase in WSS, which contributes to the rupture of microemboli trapped by IVCF<sup>31,32</sup>. Among the three helical structure IVCFs, EPF, due to its radial expansion structure, has a relatively close fit with blood vessels, and the helical structure in this part loses its ability to induce blood rotation in part. In CPF and SPF, because there are more suspended parts of the helical structure, blood flow contacts it in a large area, resulting in a strong helical flow effect and thus the best dissolution effect on thrombi. In SPF, the structure of the proximal end is gradually tightened, which has a certain obstruction effect on blood flow, so that the degree of blood whirling flow is slightly smaller. Therefore, we believe that CPF is the best in terms of its ability to dissolve thrombi.

Changes in IVCF blood flow velocity were reflected in the streamline (Fig. 4). We believe that in CPF and SPF, the larger degree of blood helicity is the key factor leading to this phenomenon. When blood passes through them, it will flow from the upstream position with a sparse helical structure to the downstream part with a dense helical structure in a helical state. In the LPF, since the direction of blood flow is not affected, the area with increased blood flow velocity will not be concentrated. Because most of its structure is suspended in the blood vessels, the cross-sectional area of the vascular channel is reduced, and the blood flow velocity through its various parts will increase. EPF has a radial expansion structure and sparse helical structure, and the blood flow through the area is large, so the blood flow velocity is small.

As shown in Fig. 7a,b, whether the blood flow velocity is 0.06 m/s or 0.1 m/s, the part near the center of the proximal end of the IVCF receives a much larger WSS than the other parts. In fact, this is related to the Poiseuille distribution of the fluid in the pipeline<sup>33</sup>. The closer the blood flows to the center of the pipeline, the faster the flow velocity, and WSS is positively correlated with the flow velocity<sup>34</sup>. First, the high WSS on the IVCF surface promotes the dissolution of larger thrombi (blood clots) captured by IVCFs, which is advantageous. However, at high WSS on the IVCF surface, platelets may be activated, causing platelet aggregation to form clots, but in this study, WSS was within a safe range<sup>35,36</sup>. The distribution of WSS on the IVCF is closely related to the shape of the

IVCF. The more suspended parts of IVCF in the blood vessel, the more structures exposed to high-speed blood flow near the vascular central axis, and the larger WSS will be. For EPF, because a large part of its structure is closely attached to the blood vessel wall, the WSS is relatively small. In addition, compared with LPF with linear structures, the existence of helical structures increases WSS in IVCFs to a certain extent<sup>36</sup>.

IVCF displacement can lead to some serious complications, such as osteodiskitis of the lumbar spine and cardiac tamponade<sup>37,38</sup>. The drag force exerted by the blood on the IVCF can be used to assess the risk of axial displacement of the IVCF material under the action of blood flow. As shown in Fig. 8, It is clear that EPF is least affected by drag at both blood flow velocities, indicating that it has the least risk of displacing under the influence of blood flow. The analysis shows that this is the result of the combination of a large gap and small suspension structure. Unfortunately, the size of the IVCF gap directly affects the thrombus trapping ability. EPF may not have an advantage in capture efficiency.

Under the impact of blood flow, IVCF has a blocking effect on blood flow, and this blocking effect is the main cause of local stress increase, which directly leads to blood vessel deformation and thus brings the risk of blood vessel perforation. In the investigation of the total deformation of the blood vessel wall (Fig. 9), SPF and CPF, due to their relatively large contraction degree, reduced the blood transmission rate at the proximal end of the IVCF, resulting in high local blood pressure and compression of the blood vessel wall. LPF, due to the small contact area between its support rod and the blood vessel wall, increases the pressure per unit area and causes deformation of the blood vessel wall. Due to the radial expansion of the support structure of EPL, the support rods are relatively sparse compared with other IVCFs, and the blood transmission area is large, so the local stress caused by blood flow is minimal and the local blood vessel wall deformation is minimal.

In in vitro experiments, we tested the thrombus trapping ability of four IVCF types, from EPF to CPF to SPF. With a decrease in the dilation degree, the density of the helical support rod increases, and the trapping ability of the IVCF for small thrombi increases. However, with the decrease in dilation degree, the contact area between the IVCF and the vascular wall also decreases. This is not good for IVCF to be permanently fixed in the inferior vena cava. When blood flow impinges on IVCF at a certain speed, CPF, SPF and LPF all shift to varying degrees, and the LPF with the smallest contact area with the vascular wall is even flushed out, resulting in complete failure of its function. Such displacement is unacceptable in clinical treatment. The occurrence of this displacement will bring many complications to the patient, and the displaced IVCF needs to be removed through surgery, which increases the pain of the patient<sup>14,38</sup>. Due to its radial expansion, EPF is firmly fixed at the initial position. In the evaluation of drag force by numerical simulation, EPF has the lowest drag force at both flow rates. In the in vitro experiment, EPF does not show observable displacement under the impact of water flow, and the results of numerical simulation are consistent with those of in vitro experiment. As for LPF, although its drag force is also at a low level, it still completely disengages under the impact of water flow in vitro experiments, which is related to its fixed stability. The small contact area between LPF and blood vessel wall leads to its poor stability. Therefore, in our study, EPF is the IVCF with the least displacement risk.

For fixation of the IVCF, traditional filters are fixed in the blood vessel by the barbs at the end of the support rod<sup>39</sup>. In this study, the IVCF is fixed in the blood vessel by using the rebound stress after compression of the IVCF support rod, and the curved contact surface allows the elastic stress to be uniformly distributed on the contact surface of the IVCF with the blood vessel wall. There will not be any area of concentration of the stress, which will reduce the risk of perforation of the blood vessel.

## Conclusion

According to the CFD results, we can clearly see that compared with the direct support structure LPF, the helical structure of IVCF does have the function of inducing blood helical flow, and this helical flow of blood can effectively prevent the deposition of inferior vena cava thrombosis. This helical flow state of blood brings additional WSS to accelerate the dissolution of trapped thrombi and blood clots. Comparing the ability of the three helical IVCF structures to induce blood rotation, EPF was slightly lower than CPF and SPF, but for IVCF with a longer placement time, the stress on the blood vessel wall and the risk of displacement should be considered. With respect to EPF, the risk of vessel perforation due to radial vessel stress (deformation) and displacement due to blood flow resistance was lowest. However, it must be taken into account that excessive spacing between the support legs will inevitably lead to a lower rate of thrombus capture. CPF and SPF caused some deformation of the blood vessel wall to some extent, but at the same time, they also brought better hemodynamic performance to the blood flow in the IVC. The greater the contact surface of the IVCF with the inner wall of the blood vessel, the less the risk of shedding displacement (possibly due to radial elastic forces and axial friction). In summary, we proposed a helical IVCF constructed based on 3D printing. This helical structure can indeed induce blood rotation to accelerate clot dissolution. Among the three helical IVCFs, after a comprehensive performance evaluation, we believe that the EPF has the most balanced performance, and this concept of blood flow induced by a self-supporting structure can provide a certain reference for the prevention of DVT by IVCF.

## Data availability

All data generated or analyzed during this study are included in this published article.

Received: 18 November 2023; Accepted: 30 July 2024

Published online: 02 August 2024

## References

- Zhang, Z., Yang, Z., Chen, M. & Li, Y. Compound heterozygous protein C deficiency with pulmonary embolism caused by a novel PROC gene mutation: Case report and literature review. *Medicine* **101**(42), e31221 (2022).

2. Jamil, A. *et al.* Current interventional therapies in acute pulmonary embolism. *Progress Cardiovasc. Diseases* **69**, 54–61 (2021).
3. Huang, C. *et al.* Fully automated segmentation of lower extremity deep vein thrombosis using convolutional neural network. *BioMed. Res. Int.* **2019**, 3401683 (2019).
4. Wadajkar, A. S. *et al.* Deep vein thrombosis: Current status and nanotechnology advances. *Biotechnol. Adv.* **31**(5), 504–513 (2013).
5. Chappell, F. M. *et al.* D-Dimer tests for the diagnosis of deep venous thrombosis in symptomatic hospital outpatients with a clinical prediction rule. *Cochrane Database Syst. Rev.* **2016**(9), CD012356. <https://doi.org/10.1002/14651858.CD012356.eCollection> (2016).
6. Huang, W. *et al.* A case of pulmonary embolism with bad warfarin anticoagulant effects caused by *E. coli* infection. *Open Life Sci.* **18**(1), 20220539 (2023).
7. Xu, S. *et al.* Model predictions of deformation, embolization and permeability of partially obstructive blood clots under variable shear flow. *J. R. Soc. Interface.* **14**(136), 20170441 (2017).
8. Lin, Z. *et al.* Nomogram for predicting deep venous thrombosis in lower extremity fractures. *BioMed. Res. Int.* **2021**, 9930524 (2021).
9. Li, Q., Yu, Z., Wang, J., Chen, X. & Li, L. Long-term prognostic analysis of early interventional therapy for lower extremity deep venous thrombosis. *Exp. Therap. Med.* **12**(6), 3545–3548 (2016).
10. He, J. *et al.* The application of inferior vena cava filters in orthopedics and current research advances. *Front. Bioeng. Biotechnol.* **10**, 1045220 (2022).
11. Xiao, L. *et al.* Transcatheter thrombolytic therapy for symptomatic thrombo-occlusion of inferior vena cava filter. *Exp. Therap. Med.* **5**(2), 533–538 (2013).
12. Shen, H. *et al.* Optimal cytoreductive surgery for underlying ovarian cancer associated with deep venous thrombosis without placement of inferior vena cava filter: A case report and literature review. *Oncol. Lett.* **10**(4), 2579–2583 (2015).
13. Eight-year follow-up of patients with permanent vena cava filters in the prevention of pulmonary embolism: The PREPIC (Prevention du Risque d'Embolie Pulmonaire par Interruption Cave) randomized study. *Circulation.* **112**(3), 416–422 (2005).
14. Zhou, M., Qi, L. & Gu, Y. Successful retrieval of dislocated inferior vena cava filter using double vascular sheaths docking technology: Case report. *Thromb. J.* **19**(1), 56 (2021).
15. Li, M., Wang, J., Huang, W., Zhou, Y. & Song, X. Evaluation of hemodynamic effects of different inferior vena cava filter heads using computational fluid dynamics. *Front. Bioeng. Biotechnol.* **10**, 1034120 (2022).
16. Yang, C. *et al.* Design and evaluation of a novel biodegradable inferior vena cava filter. *J. Biomater. Appl.* **33**(8), 1060–1069 (2019).
17. Clements, W. Inferior vena cava filters in the asymptomatic chronically occluded cava: To remove or not remove?. *CardioVasc. Int. Radiol.* **42**(2), 165–168 (2019).
18. Li, R. L., Voit, A., Commander, S. J., Mureebe, L. & Williams, Z. Mechanical thrombectomy of inferior vena cava filter-associated caval thrombosis using FlowTriever and ClotTriever systems. *J. Vasc. Surg. Venous Lymphatic Disorders.* **11**(6), 1175–1181 (2023).
19. Chen, Z., Zhan, F., Fan, Y. & Deng, X. A novel way to reduce thrombus build-up in vena cava filters. *Catheterization Cardiovasc. Intervent.* **78**(5), 792–798 (2011).
20. Huang Zhang, P. *et al.* The mechanics of spiral flow: Enhanced washout and transport. *Artif. Organs* **43**(12), 1144–1153 (2019).
21. De Nisco, G. *et al.* The atheroprotective nature of helical flow in coronary arteries. *Ann. Biomed. Eng.* **47**(2), 425–438 (2019).
22. Chen, Y. *et al.* Improvement of hemodynamic performance using novel helical flow vena cava filter design. *Sci. Rep.* **7**, 40724 (2017).
23. Chen, Y., Deng, X., Shan, X. & Xing, Y. Study of helical flow inducers with different thread pitches and diameters in vena cava. *PLoS One* **13**(1), e0190609 (2018).
24. Moshfegh, A., Javazdegan, A., Zhang, Z., Afrouzi, H. H. & Omid, M. Effect of aortic spiral blood flow on wall shear stress in stenosed left main coronary arteries with varying take-off angle, stenosis severity and eccentricity. *J. Mech. Sci. Technol.* **32**(8), 4003–4011 (2018).
25. Rajan, A., Makary, M. S., Martyn, T. D. & Dowell, J. D. Computational evaluation of inferior vena cava filters through computational fluid dynamics methods. *Diagnostic Interventional Radiol. (Ankara, Turkey).* **27**(1), 116–121 (2021).
26. Gallagher, M. B., Aycock, K. L., Craven, B. A. & Manning, K. B. Steady flow in a patient-averaged inferior vena cava-Part I: Particle image velocimetry measurements at rest and exercise conditions. *Cardiovasc. Eng. Technol.* **9**(4), 641–653 (2018).
27. Jiang, X. D., Ye, S. L., Zhang, M., Li, X. Q. & Sun, L. L. Clinical implications of hemodynamic analysis for the three-dimension iliac vein model with different stenosis. *Heliyon* **9**(2), e13681 (2023).
28. Riley, J. M. *et al.* In vitro clot trapping efficiency of the FDA generic inferior vena cava filter in an anatomical model: An experimental fluid-structure interaction benchmark. *Cardiovasc. Eng. Technol.* **12**(3), 339–352 (2021).
29. Liu, J., Tian, L., Wang, S. & Luo, Z. Study of hepatic vascular dynamics based on symmetrical pulsating perfusion. *Ann. Transplant.* **24**, 214–222 (2019).
30. Dyverfeldt, P., Trenti, C., Ziegler, M., Bjarnegård, N. & Lindenberg, M. Helical flow in tortuous aortas and its relationship to turbulence: A whole-aorta 4D flow MRI study. *Front. Cardiovasc. Med.* **10**, 1124604 (2023).
31. Liu, X. *et al.* Bioinspired helical graft with taper to enhance helical flow. *J. Biomech.* **49**(15), 3643–3650 (2016).
32. Kulcsár, Z. *et al.* Flow diversion treatment: Intra-aneurysmal blood flow velocity and WSS reduction are parameters to predict aneurysm thrombosis. *Acta Neurochirurgica* **154**(10), 1827–1834 (2012).
33. Connolly, S., McGourty, K. & Newport, D. The in vitro inertial positions and viability of cells in suspension under different in vivo flow conditions. *Sci. Rep.* **10**(1), 1711 (2020).
34. Odagiri, K. *et al.* Noninvasive evaluation of pulmonary arterial blood flow and wall shear stress in pulmonary arterial hypertension with 3D phase contrast magnetic resonance imaging. *SpringerPlus* **5**(1), 1071 (2016).
35. Hathcock, J. J. Flow effects on coagulation and thrombosis. *Arterioscl. Thromb. Vasc. Biol.* **26**(8), 1729–1737 (2006).
36. Ascuitto, R., Ross-Ascuitto, N., Guillot, M. & Celestin, C. Computational fluid dynamics characterization of pulsatile flow in central and Sano shunts connected to the pulmonary arteries: Importance of graft angulation on shear stress-induced, platelet-mediated thrombosis. *Interactive Cardiovasc. Thoracic Surg.* **25**(3), 414–421 (2017).
37. Aoun, S. G. *et al.* Osteomyelitis of lumbar spine due to migrated fractured inferior vena cava filter. *World Neurosurg.* **113**, 298–303 (2018).
38. Haddadian, B., Shaikh, F., Djelmami-Hani, M. & Shalev, Y. Sudden cardiac death caused by migration of a trapease inferior vena cava filter: Case report and review of the literature. *Clin. Cardiol.* **31**(2), 84–87 (2008).
39. Hoekstra, A., Hoogeveen, Y., Elstrodt, J. M. & Tiebosch, A. T. M. G. Vena cava filter behavior and endovascular response: An experimental in vivo study. *CardioVasc. Interventional Radiol.* **26**(3), 222–226 (2003).

## Acknowledgements

The authors thank Liu Ming, Ph. D for providing technical support.

## Author contributions

ZM, LM and CY conceived of the study and participated in its design and coordination. LM and HYX contributed to the acquisition of the data and participated in the analysis and interpretation of data. LM, HYX and LQ participated in writing the manuscript. All authors have read and approved the final manuscript.

## Funding

This research was supported by Zhejiang Provincial Natural Science Foundation of China under Grant (No. LZ22A020005). This research was also supported by the Scientific Research Project of Beijing Institute of Economics and Management (No. 22BSA01) and the National Natural Science Foundation of China-Youth Science Fund (No. 82204538).

## Competing interests

The authors declare no competing interests.

## Additional information

**Correspondence** and requests for materials should be addressed to M.L., M.Z. or Y.C.

**Reprints and permissions information** is available at [www.nature.com/reprints](http://www.nature.com/reprints).

**Publisher's note** Springer Nature remains neutral with regard to jurisdictional claims in published maps and institutional affiliations.



**Open Access** This article is licensed under a Creative Commons Attribution-NonCommercial-NoDerivatives 4.0 International License, which permits any non-commercial use, sharing, distribution and reproduction in any medium or format, as long as you give appropriate credit to the original author(s) and the source, provide a link to the Creative Commons licence, and indicate if you modified the licensed material. You do not have permission under this licence to share adapted material derived from this article or parts of it. The images or other third party material in this article are included in the article's Creative Commons licence, unless indicated otherwise in a credit line to the material. If material is not included in the article's Creative Commons licence and your intended use is not permitted by statutory regulation or exceeds the permitted use, you will need to obtain permission directly from the copyright holder. To view a copy of this licence, visit <http://creativecommons.org/licenses/by-nc-nd/4.0/>.

© The Author(s) 2024